ARTICLE   OPEN

Check for updates

Sh3rf3 Deficiency drives autism-like behaviors via presynaptic dysfunction in mice

Yuting Yuan [1,8], Yang Li[2,3,4,8], Fuqiang Yang [1,5,8], Yisheng Jiang[5,8 ✉], Yuanyuan Ding [6], Ying Xiao[6], Xili Zhu[7], Xingmei Shu[7], Xiahe Huang[1], Yingchun Wang[1], Shuli Zhang[2], Jianyuan Sun[2,3,4] and Zhiheng Xu [1,5 ✉]

Autism spectrum disorder (ASD) is a prevalent and complex neurodevelopmental disorder with a strong genetic basis. Although SH3RF3 has been identified as an ASD candidate gene, its biological function and pathophysiological mechanisms remain elusive. Here, we reveal that SH3RF3 functions as an essential scaffold protein that facilitates presynaptic vesicle docking. Mechanistically, it orchestrates the formation of a molecular complex between the kinase BRSK1/SAD-B and the ASD-associated active zone protein RIM1. Genetic ablation of Sh3rf3 disrupts this protein-protein interaction, leading to reduced RIM1 phosphorylation. This perturbation triggers synaptic dysfunctions, marked by a substantial reduction in both total synaptic vesicle (SV) density and readily releasable pool size, coupled with delayed SV replenishment kinetics. These deficits ultimately impair excitatory synaptic transmission in the prefrontal cortex, disturb the excitatory-inhibitory (E/I) balance, and elicit autistic-like behaviors in mice. Notably, prefrontal cortex-specific restoration of Sh3rf3 reverses behavioral and functional deficits in knockout mice. Furthermore, our characterization of the SH3RF3 interactome reveals a shared molecular network encompassing ASD-risk genes, indicating that synapse-targeted therapies may have broad applicability.

INTRODUCTION

Autism spectrum disorder (ASD) is a complex neurodevelopmental disorder characterized by impaired social interaction, communication, and stereotyped repetitive behaviors and its prevalence has been steadily rising in recent years [1]. Many genes linked to ASD have been identified [2–4], and some of the animal models harboring mutations in these genes exhibit synaptic dysfunctions and recapitulate ASD-like behaviors [5–9]. These findings support the hypothesis that synaptic dysfunction is a central mechanism in ASD pathophysiology [6, 7, 9–11]. Notably, ASD mouse models frequently display abnormal excitatory synaptic transmission and social deficits [6, 7, 12, 13]. However, the synaptic roles of many ASD-related genes remain uncharacterized, and a definitive causal link between synaptic dysfunction and ASD-like behaviors remains to be conclusively established.

Synaptic transmission is a tightly regulated process essential for neuronal communication. Neurotransmitter release, a critical step mediated by exocytosis, is spatiotemporally controlled [14]. This release is restricted to presynaptic active zone- specialized structures composed of multidomain proteins including RIM, Munc13, RIM-BP, Piccolo/Bassoon, ELKS, and Liprin-α. [15, 16]. These protein assemblies ensure the sub-millisecond precision in synaptic vesicle exocytosis. Among them, the ASD associated protein, RIM1, serves dual functions: mediating synaptic vesicle

(SV) docking/priming while anchoring voltage-gated calcium channels at the active zones [17–21]. BRSK1, also named SAD-B, a brain-enriched serine/threonine kinase associated with active zones, regulates synaptic vesicle release by phosphorylating synaptic proteins such as RIM1 [22]. This phosphorylation is crucial for maintaining synaptic plasticity and neurotransmission fidelity [22–24].

SH3RF3 (SH3 domain containing ring finger 3, also known as POSH2), contains four SH3 domains for protein-protein interactions and a ring finger domain conferring E3 ubiquitin ligase activity, which may target itself and other proteins for proteasomal degradation [25]. SH3RF3 can interact with PAK2 and RAC1 through its SH3 domains and functions as a scaffold to promote the JNK signaling pathway [25, 26]. SH3RF3 belongs to the SH3RF family, alongside SH3RF1 and SH3RF2. Intriguingly, we have shown that knockout of either Sh3rf1 or Sh3rf2 in mice causes autistic-like behaviors [27, 28], and mutations in SH3RF3 have also been reported in ASD patients [29–32], strongly implicating SH3RF3 as an ASD risk gene. However, its biological functions and role in ASD pathogenesis remain unexplored.

Here, we show that SH3RF3 acts as a scaffold protein to promote the interaction between BRSK1/SAD-B and RIM1 and the phosphorylation of RIM1 by BRSK1/SAD-B. Sh3rf3 deletion reduces RIM1 phosphorylation, diminishes readily releasable pool, and

[1]Institute of Genetics and Developmental Biology, University of Chinese Academy of Sciences, Chinese Academy of Sciences, Beijing 100101, China. [2]Institute of Biophysics, University of Chinese Academy of Sciences, Chinese Academy of Sciences, Beijing 100101, China. [3]Brain Cognition and Brain Disease Institute, Shenzhen Institutes of Advanced Technology, Chinese Academy of Sciences, Shenzhen 518055, China. [4]Shenzhen University of Advanced Technology, Shenzhen 518107, China. [5]Department of Neurology, the Second Affiliated Hospital, School of Medicine, Zhejiang University, Hangzhou 310009, China. [6]Center for Translational Neural Regeneration Research, Sir Run Run Shaw Hospital, School of Medicine, Zhejiang University, Hangzhou 310016, China. [7]Institute of Zoology, Chinese Academy of Sciences, Beijing 100101, China. [8]These authors contributed equally: Yuting Yuan, Yang Li, Fuqiang Yang, Yisheng Jiang. ✉email: ysjiang01@zju.edu.cn; zhxu@genetics.ac.cn

slows vesicle replenishment rates. These deficits may impair excitatory synaptic transmission, disrupt excitatory-inhibitory balance, and result in autistic-like phenotypes in mice.

MATERIALS AND METHODS

Animals
The *Sh3rf3* knock-out mouse model was generated by Beijing Biocytogen Co., ltd. To obtain GFP-labeled neurons, the *Sh3rf3* KO mice were crossed with *Thy1-GFPm* mice (Gift from Weixiang Guo, IGDB, CAS). *Sh3rf3-3 × flag* knock-in mouse model was generated by Jiangsu GemPharmatech. All mice were in C57BL/6 background.

Mice for behavioral tests were housed in groups on a 12 h light/dark cycle, with free access to food and water except during behavioral testing. All behavioral tests were performed during the light phase of the cycle between 09:00 and 17:00. Housing temperature ranged from 21 to 23 °C. Housing humidity ranged from 30% to 70%. Male and female mice at 6-12 weeks of age were used for the behavior tests as indicated. Experimenters were blind to the genotype when behavioral tests were carried out. No exclusion or additional sampling was performed prior to the experiments. For the genotype of mice, we sequenced the mouse DNA to verify the successful establishment of both KO and KI mouse models using CRISPR/CAS9. Tail biopsies were used to extract genomic DNA for genotyping. The primer sequences are listed in Table S1.

In vivo knockdown/overexpression modulation
To knock down *Sh3rf3*, short-hairpin RNA (shRNA) sequence (CCTGGCTCTCTATGCATACAA) and ctrl shNC2 RNA (CCTAAGGT-TAAGTCGCCCTCG) were cloned into GFP-tagged adeno-associated virus (AAV) -vector (Addgene) under the control of U6 promoter. Viral particles (titer: $5.23 × 10^{12}$ vg/mL) were produced by the Obio Technology (Shanghai) Corp., Ltd. To re-express *Sh3rf3*, the *Sh3rf3* sequence (GeneID:237353) was cloned into the pAAV-hSyn-EGFP-P2A-tWPA vector. Viral particles (titer: $4.92 × 10^{12}$ vg/mL) were produced by the Obio Technology (Shanghai) Corp., Ltd.

Sh3rf3 shRNA/overexpression AAV was bilaterally injected into the medial PFC (2.43 mm anterior to bregma; 0.4 mm lateral; and 2 mm dorsal to ventral; 0.5 μL each side) of WT mice (4-5 weeks old). In brief, mice were anesthetized and placed on a stereotaxic apparatus (RWD Life Science Co., Ltd). The injection was carried out with a Hamilton syringe (needle gauge 31) at a speed of ~0.1 μL/min, and needles were kept in place for an additional 10 min.

Quantitative real-time RT-PCR
RNA was extracted by Trizol, 1.5 μg RNA was employed for cDNA reverse transcription, and SYBR Green mixture was used for the reaction system. The specificity was determined through the melt curve. All data were normalized by GAPDH transcript and calculated using the ΔΔCq method. Fold changes in the target genes were determined by: Fold change $= 2^{-Δ(ΔC_T)}$, where $ΔCT = C_{T(target)} - C_{T(GAPDH)}$, and $Δ(ΔC_T) = ΔC_{T(EG\ group)} - ΔC_{T(CG\ group)}$. C_T (threshold cycle) is defined as the fractional cycle number at which the fluorescence reaches $10 ×$ the standard deviation of the baseline. A total reaction mixture of 20 μl was amplified in a 96-well thin-wall PCR plate (Bio-Rad) using the following PCR cycling parameters: 95 °C for 5 min followed by 40 cycles of 95 °C for 30 s, 51 °C for 30 s, and 72 °C for 60 s. The primer sequences are listed in Table S2.

Immunofluorescence analysis
Mice were anesthetized by tribromoethanol and perfused with a phosphate buffer solution (PBS) followed by 4% paraformaldehyde (PFA). Brains were postfixed in 4% PFA for 24 hours and submerged in 30% sucrose in PBS for 48 hours. For immunofluorescence analysis, frozen PFC sections were permeabilized with Triton X-100 (0.2% in PBS) following blocking buffer (10% FBS and 5% BSA in PBS), incubated with primary antibodies overnight at 4 °C, then incubated with secondary antibody in conjunction with Alexa fluor®. The antibodies are listed in Table S3. Images were photographed by LSM 800 (Carl Zeiss) confocal microscope and analyzed by ImageJ (1.8.0).

Western blot
Frozen brain samples or cultured HEK293 cells kept in our lab were lysed in ice-cold buffer (50 mM Tris-HCl pH 7.4, 150 mM NaCl, 1% NP40, 0.5% DOC,

1 mM EDTA) with protease inhibitors. After 30 minutes on ice, samples were sonicated (100 W, 5 s, 3 pulses). Lysates were centrifuged (13,000 × g, 15 min, 4 °C), and supernatants were boiled in SDS loading buffer (95 °C, 5 min). Proteins were separated by 8 or 10% SDS-PAGE and transferred to nitrocellulose membranes. Membranes were blocked with 5% skim milk (1 h, RT), incubated with primary antibodies overnight at 4 °C, then with HRP-linked secondary antibodies (1 h, RT). Signals were detected using ECL and analyzed with SageCapture/Lane 1D software. β-actin/GAPDH served as loading controls. The antibodies were listed in Table S4.

Immunoprecipitation/IP-MS
Frozen PFC samples were lysed in buffer (20 mM Tris-HCl pH 7.4, 10 mM HEPES pH 7.4, 50 mM NaCl, 0.5 mM EDTA, 0.5 mM EGTA, 0.5% NP-40) containing protease inhibitors (Roche) and 1 mM PMSF (30-40 min, 4 °C), then sonicated (100 W, 5 sec, 3 pulses). Lysates were centrifuged (13,000 × g, 15 min, 4 °C), and protein concentrations were measured using a BCA kit (Thermo). For immunoprecipitation, 2 mg protein was incubated with antibody-bound Protein A/G beads (pre-coupled for 2 h at 4 °C) overnight at 4 °C. Precipitates were washed six times with lysis buffer.

HEK293 cells were cultured in DMEM with 10% FBS and antibiotics (50 U/mL penicillin, 50 μg/mL streptomycin) at 37 °C/5% CO_2. Transfections used VigoFect per protocol. Cells were collected 24 h post-transfection and lysed in buffer (50 mM Tris-HCl pH 7.4, 100 mM NaCl, 2 mM EDTA, 1% NP-40) containing Roche protease inhibitors and 1 mM PMSF (30-40 min, 4 °C). Lysates were sonicated (100 W, 5 sec, 3 pulses), centrifuged (13,000 × g, 15 min, 4 °C), then incubated with anti-Flag/GFP beads (Lablead) for 2-4 h at 4 °C.

After incubation, the immunoprecipitates were washed five to six times with cell lysis buffer. Immunoprecipitates were eluted from the agarose by boiling in 2 × SDS Gel loading buffer (100 mM Tris-HCl, pH 6.8, 4% SDS, 0.2% romophenol blue, 20% vol/vol glycerol, 10% vol/vol 2-mercaptoethanol) and resolved by SDS-PAGE and immunoblotted with the indicated antibodies.

Subcellular fractionation
To obtain the crude membrane fractions, subcellular fractionation of the mouse brain (0.3 g) was performed as described previously with modifications [33]. In brief, brain homogenates were centrifuged at 800 × g. The supernatant (S1) was centrifuged at 9200 × g, and the resultant pellet was washed and homogenized in buffer A (4 mM HEPES pH 7.3, 0.32 M sucrose, and complete protease inhibitor) and then used as the crude membrane fraction (P2) [24]. To obtain the SM3 and PSD fractions, subcellular fractionation of the mouse brain was performed as described previously [22, 33]. In brief, the synaptosomal membrane fraction was centrifuged at 48,200 × g at 4 °C and purified on a set of sucrose density gradients consisting of 0.85, 1.0, and 1.2 M sucrose. The band between 1.0 and 1.2 M sucrose was collected and used as the SM3 fraction. This fraction contains the pre- and postsynaptic membranes plus the PSD and docked vesicles. The SM3 fraction was treated with 1% (w/v) Triton X-100 and further centrifuged at 48,200 × g at 4 °C. The supernatant is designated as the PSD-S fraction, and the pellet is designated as the PSD-P fraction [24].

6plex-tandem mass tag (TMT)- labeled quantitative proteomic analysis and phosphoproteomics assays
The samples were digested with cell lysis (0.1 M Tris-HCl pH 8.5, containing 4% sodium deoxycholate, Sigma D6750), and then sonicated (100 W, 5 s, 3 pulses). Lysates were centrifuged (13,000 × g, 15 min, 4 °C), and supernatants were boiled in SDS loading buffer (100 °C, 5 min). The protein concentrations were detected using a BCA protein assay kit (Thermo Scientific, Rockford, IL). For volcano plot and bar plots, differentially expressed phosphoproteins (up and down) were selected with the criteria $p < 0.05$ and $FC > 1.25$ or < 0.8. Several differentially expressed proteins that detected in 2 replicates were also included (up-2 and down-2). SynGO analysis was performed with differentially detected phosphoproteins (up and down) based on the website tool (https://syngoportal.org/) [34], and the enriched GO terms were listed in Table S8.

Phosphate affinity chromatography
The samples were digested with cell lysis (50 mM Tris-HCl pH 7.4, 150 mM NaCl, 1% NP40, 0.5% DOC, 1 mM EDTA pH 8.0, supplied with 2 mM PMSF, protein inhibitors and phosphatases inhibitors cocktails). Keep on ice for 30 min; ultrasonication for 100 W, 5 s, 3 pulses. Cell lysates were centrifuged at 13,000 × g for 15 min at 4 °C. A homemade spin-centrifuge

microtube unit is prepared. Place 40 μL suspension (50% v/v) of Phos-tagTM agarose (20 μL swelled gel, Zn^{2+}-boud form) into the 0.5-mL tube of the unit. Centrifuge the spin column unit for 20 s and the filtrate is discarded. Apply 40 μL of a balancing buffer (0.10 mol/L Tris-CH3COOH (pH 7.5), 1.0 mol/L CH3COONa, and 10 μmol/L Zn(CH3COO)₂) in the 0.5-mL tube. After 5 min, centrifuge the unit for 20 s. and the filtrate is discarded. Wash the gel three times with 40 μL of a binding/washing buffer (0.10 mol/L Tris-CH3COOH (pH 7.5) and 1.0 mol/L CH3COONa) by the same centrifugal method. Apply 10 μL of a cell lysate sample, which contains less than 20 μg proteins. After equilibration for 5 min, centrifuge the spin column and collect a flow-through fraction as the filtrate. Wash the phosphoprotein-bound gel with 0.10 mL of the binding/washing buffer, centrifuge the unit for 20 s to collect a washing fraction. After addition of distilled water (40 μL or more) to the phosphoprotein-bound gel, the whole swollen gel slurry is completely transferred to a new 1.5-mL tube. The tube is centrifuged for 20 s, and the supernatant fluid is discarded. To the remaining gel at the bottom of the tube, 10 μL of a sample-loading SDS buffer is added. The tube is heated for 5 min at 95 °C. Transfer the whole suspension of the gel to a sample well of an SDS-PAGE gel [35, 36].

Dendritic arborization and spine morphology

For the morphometric analysis of dendritic protrusions, we used GFP as an unbiased cell-fill. Maximum image projections and three-dimensional projections used in spine density calculations were rendered with the Imaris (Bitplane) from confocal z-series images. All morphological experiments were repeated at least three times.

In brief, coronal brain sections (100 μm) were prepared from *Sh3rf3* KO mice with *Thy1-GFPm* and littermate controls. The investigator was blind to genotype during image acquisition and analysis of spine morphology. Synapse density is presented as the number of above-threshold puncta per 10 μm of dendrite. For dendritic analysis, both apical and basal processes of PFC pyramidal neurons were analyzed. Three-dimensional (3D) reconstructions of entire dendritic trees of each GFP⁺ neuron were analyzed for total dendritic length and dendritic complexity by Sholl analysis. Spine density was measured as described previously using the measurement tool in ImageJ software. Spines were classified into four groups based on the algorithm as follows: mushroom: length (spine) < 3 μm and mean width (head) ≥ mean width (neck) × 2; stubby: length (spine) < 1 μm; long thin: mean width (head) ≥ mean width (neck); filopodia: length (spine) > 2 μm.

Transmission electron microscopy (TEM) and statistical analysis

Transmission EM was performed in the PFC area of *Sh3rf3* KO mouse and its control littermate (both at P45-50), using standard fixation and resin embedding procedures as previously described [37]. Coronal brain sections (200 μm thickness) containing the PFC were prepared and transferred to freshly prepared solution containing 2.5% glutaraldehyde and 2% paraformaldehyde for at least 1 h at room temperature. The fixed sections were stored in 4 °C refrigerator overnight. On the next day, the sections were trimmed into ~ 0.2 mm³ cube containing the PFC under a stereoscope. The sections were postfixed in 1% osmium tetroxide for 1.5 h, dehydrated in an ascending series of ethanol [30, 50, 70, 85, 95, and 100% (vol/vol)], and stored in epoxy (EPON 812) overnight. The sections were then embedded in epoxy resin at 60 °C for 48 h of polymerization. The semithin sections (500 nm thickness) were stained with Toluidine blue and the layer 2/3 of the PFC was confirmed by bright-field microscope. Then the resin was further trimmed until only the layer 2/3 of the PFC was included. The ultrathin sections (50 nm thickness) were cut by Leica EM UC6 tramicrotome and mounted on Formvar-coated slot grids. After poststaining with 2% (w/v) uranyl acetate and 8% (w/v) lead citrate, the ultrathin sections were examined on a Tecnai Spirit TEM (FEI) at 120 kV. Imaging was focused on asymmetric synapses, which are known to be glutamatergic, based on their morphological hallmarks: a prominent postsynaptic density and spherical synaptic vesicles. Data were analyzed with IMOD 4.11 (University of Colorado).

Brain Slice Preparation

Brain slices were prepared from control and *Sh3rf3* KO mice. Coronal slices containing the PFC (200 μm thick) were prepared from mice from 8 to 11 weeks by using a vibratome slicer (Leica, Germany) in a chilled (0–4 °C) cutting solution containing 120 mM Choline-Cl, 28 mM NaHCO3, 1.25 mM NaH2PO4, 2 mM KCl, 25 mM glucose, 1 mM CaCl2, 8 mM MgCl2, bubbled with 95% O2 and 5% CO2. Slices were transferred to artificial cerebrospinal fluid (aCSF) containing 125 mM NaCl, 2.5 mM KCl, 2 mM CaCl2, 1 mM MgSO4, 1.25 mM NaH2PO4, 26 mM NaHCO3, and 20 mM glucose bubbled with 95% O2 and 5% CO2 and incubated at 34 °C for 45 min. After recovery, brain slices in aCSF were kept at room temperature for at least 30 min before electrophysiological recording [38].

Electrophysiology

The electrophysiology was adapted as described previously [12, 39]. Visually guided (infrared DIC video microscopy and water-immersion X40 objective) whole-cell recordings were obtained from visually identified layer 5 pyramidal neurons of the PFC, with patch pipettes (2.5-4.5 MΩ) pulled from borosilicate capillary glass using a Sutter P97 puller (Sutter Instrument, Novato, CA, USA). Recordings were obtained with an EPC10 amplifier (HEKA Elektronik, Lambrecht, Rhineland-Palatinate, Germany) or Multiclamp 700B amplifier, Digidata 1550B converter and pClamp 10.7 software (Axon Instruments), sampled at 20 or 50 kHz. All data were analyzed with Igor Pro-6.2 (WaveMetrics). During recordings, the chamber containing brain slice was continuously perfused with aCSF solution bubbled with 95% O2 and 5% CO2 at room temperature.

mEPSC, sEPSC, evoked EPSCs, paired-pulse ratio, I/E ratio and a train of EPSCs were recorded with an internal solution containing (in mM): 140 Cs-gluconate, 15 HEPES, 0.5 EGTA, 2 TEA-Cl, 2 MgATP, 10 phosphocreatine, 2 QX 314-Cl, pH was adjusted to 7.2 with CsOH. mEPSC, sEPSC, evoked EPSCs, paired-pulse ratio and a train of EPSCs were recorded with membrane potential clamped at −70 mV in the present of 20 μM picotoxin (PTX) in aCSF to block GABAergic synaptic transmission. An additional 1 μmol/L tetrodotoxin was added to aCSF for recording mEPSC. Electrical stimulation was delivere via a bipolar electrode positioned in layer 2/3 of the PFC. Electrical output was controlled by a programmable pulse stimulator (Master-8, A.M.P.I.) For measuring the paired-pulse ratio, double stimulation pulses were delivered at varying interpulse intervals of 20 ms, 50 ms, 100 ms, and 500 ms. For measuring I/E ratio, EPSCs and IPSCs were recorded at holding potential of −30 mV and 0 mV respectively. A train of EPSCs were recorded under 20 Hz stimulation. sIPSCs were recorded with an internal solution containing (in mM): 140 CsCl, 1 BAPTA, 10 HEPES, 5 MgCl2, 5 Mg-ATP, 0.3 Na3GTP, 10 QX 314-Cl, pH was adjusted to 7.3 with CsOH. 50 μM D-(-) − 2-amino-5-phosphonopentanoic acid (D-APV) and 10 μM 6-cyano-7-nitroquinoxaline-2,3-dione (CNQX) were applied in aCSF to block AMPAR- and NMDAR-mediated synaptic transmission with holding potential of -70 mV. Action potentials were evoked by postsynaptic current injection (500 ms duration, ranging from -100 pA to 300 pA in 20 pA increments) with an internal solution containing (in mM): 125 K-gluconate, 20 KCl, 4 MgATP, 10 Na2-phosphocreatine, 0.3 GTP, 10 HEPES, and 0.5 EGTA (pH 7.2 adjusted with KOH).

Behavioral tests

Three-chamber test. The three-chamber apparatus consisted of a transparent acrylic box with a removable floor and partitions dividing the box into three equally sized chambers. Each chamber could be closed and opened with a door. Age-matched wild-type mice of the same sex were used as Strangers 1 and 2. The test mice were put in the middle chamber and left to habituate for 10 min, while Stranger 1 was introduced into a wire cage in the left chamber and an empty wire cage on the right chamber. Then the test mice were allowed to explore freely all three chambers for a 5-minute session. Following this, Stranger 2 was introduced into the previously empty wire cage and the test mouse was allowed to explore all three chambers for a 5 min session freely. Time spent in each chamber was recorded.

Habituation-Novelty recognition task. Social recognition deficits in ASD often manifest as impaired face identity recognition, particularly with delayed intervals (seconds to minutes). To model this, we assessed social recognition in juvenile mice (P55-60) using a 10-minute inter-trial interval, mirroring patient study timescales. A home cage-like environment (without grid, food, or water) was used. Mice were acclimated for 30 min pre-test. A novel same-sex mouse was introduced for 1-minute interaction, repeated at 10-minute intervals. In the 5th trial, a new novel mouse replaced the prior stimulus. For the social stimulus, the interaction was scored when the experimental mouse initiated the action and when the nose of the animal was oriented toward the social stimulus mouse only. The interaction time was used to calculate the recognition index as: (Interaction trial 5) - (Interaction trial 4) [40].

Tube test. The tube test assay was applied as described before [41]. Before the start of tube tests, mice were trained to go through the tube for 10 trials per day for 3 days. In test days, each pair of mice was released from the two ends of a tube (30 cm in length, 3 cm in diameter), met in the middle, and the mouse that retreated first from the tube is designated as the "loser". The other mouse is the winner. When no mouse retreats within 6 minutes, a side reversal repeated test will be initiated. The tubes are cleaned with 75% ethanol between trials. When compared with the chance-expected outcome (i.e., a 50:50 win-loss result), a chi-square test is applied to determine the significance of the test scores between the mice.

Marble burying test. Fill standard rodent cages with 5 cm of fresh, unscented bedding. Arrange 18 glass marbles in 6 rows (3 marbles/row) on the bedding surface. Clean marbles before each test: wash with mild detergent, rinse exhaustively in distilled-deionized water, and dry prior to each use. Deprive mice of food/water during the test. Place a single mouse in a cage corner (away from marbles) and secure the filter-top lid. Start a 30-minute timer. Allow undisturbed exploration. Count marbles buried (≥ 2/3 surface area covered by bedding) by an observer blinded to experimental groups.

Von-frey test. On the day of the experiment, turn off the lights one hour prior and maintain a quiet environment. At the start of the experiment, illuminate the area with red light to minimize stimulation and place the test mice into the testing chamber for a 10-minute acclimation period until they calm down. Use Von Frey filaments of varying diameters and stiffness (0.04 g, 0.07 g, 0.4 g, and 2 g) to stimulate the plantar surface of the mice's paws gently. Each filament is applied for 1-2 s until it slightly bends. Stimulate each paw five times on each side, with a 6-second interval between stimulations, testing in ascending order of filament force. Observe the mice's responses and assess their behavioral scores, summing up the total score from the five stimulations. A score of 2 is given for immediate licking of the stimulated paw area or sharp withdrawal or jumping of the paw; a score of 1 is given for immediate searching of the stimulated area with the paw; and a score of 0 is given for normal walking behavior.

Rearing test. To assess motor stereotypy, the repetitive rearing behavior was quantified. Each mouse was placed individually into a standard clean home-cage and allowed to habituate for 20 minutes. Its behavior was then recorded for a 10-minute test session. The total number of rearing (defined as the mouse raising its forepaws off the cage floor and standing upright on its hind legs) was manually scored by a researcher blinded to the genotype using Limelight software.

Open-field test. Mice were allowed to explore an open field arena (40 × 40 cm area, 35 cm high walls) for 10 min using a video tracking system (Limelight), followed by quantification of the distance moved and percent time spent in the center region (20 × 20 cm area).

Novel object recognition. The novel object recognition test is conducted in an open field. On the first day of the experiment, the experimental mice were allowed to freely explore two identical objects (left/right) in an open field for 10 minutes. After 24 h, replace one object with a novel one. Record the time spent interacting with each object over 10 minutes. The criterion for object contact is defined as the direct contact of the mouse's whiskers with the object.

Morris water maze. The water maze consisted of a circular water tank (120 cm diameter and 40 cm height) that contained a 6 cm circular platform and water rendered opaque by the addition of white nontoxic paint. This test contains three phases: pre-training to a visible platform; acquisition training to a hidden platform in the following 5 days (four trials per day); a probe test was performed on the 6th day with the removal of the platform. During the training phase, mice were given 60 s to find the platform, guided to the platform if necessary and remained on the platform for 30 s followed by 1 h rest before next trial. For the probe trial, mice were given 60 s to swim and the percent time spent in the target quadrant was recorded.

Quantification and statistical analysis. Sample sizes were selected based on prior similar studies. Data were reported as mean ± standard error of the mean (SEM). The statistical methods were individually annotated in the corresponding figure legends, including two-tailed Student's *t* test, two-way repeated-measures ANOVAs, Chi-square test, two-tailed Mann-Whitney test. For two-way ANOVA, multiple comparison was performed followed by FDR adjustment with BH methods. All the data for two-way ANOVA passed at least one of normality tests (D'Agostino-Pearson omnibus, Anderson-Darling, Shapiro-Wilk, Kolmogorov-Smirnov). Spearman's test for heteroscedasticity was also performed. GraphPad Prism Software was used for all analyses and $p < 0.05$ was considered statistically significant. Significance was reported as $*p < 0.05$, $**p < 0.01$, $***p < 0.001$, $****p < 0.0001$ and n. s., no significance.

RESULTS

Sh3rf3 knockout mice display autistic-like behaviors

SH3RF3 is a strong ASD candidate gene in humans (Fig. S1A). To determine whether mice with *Sh3rf3* deletion exhibit autistic-like behaviors, we generated *Sh3rf3* knockout (KO) mice (Fig. S1B) and performed an array of behavioral assays on adult male and female littermates. In the three-chamber sociability test (Fig. 1A), both male and female wild-type (WT) or KO mice preferred the chamber containing a stranger mouse over an empty cage (Fig. 1B, C). However, KO mice showed deficits in social novelty discrimination, failing to show increased interaction with the novel versus familiar mice (Fig. 1D-F). In a five-trial social habituation/recognition task, KO mice displayed significantly reduced interaction time with stranger mice and a decreased social cognitive index (WT: 22.09 ± 2.929 vs. KO: 12.63 ± 2.877 s for male mice; WT: 15.77 ± 2.36 vs. KO: 6.141 ± 3.086 s for female mice; Fig. 1G-I). The tube test revealed that WT mice outperformed KO mice in social hierarchy dominance (male: 70.59 vs. 29.41%; female: 72.73 vs. 27.27%; Fig. 1J, K).

In the open-field test, KO mice displayed less time in the center of the cage, implicating heightened anxiety levels (Fig. S2A, B). The marble burying test revealed increased repetitive digging in KO mice (WT: 6.417 ± 0.9517 vs. KO: 10.73 ± 0.6754 for male mice; WT: 3.727 ± 0.8101 vs. KO: 7.273 ± 1.236 for female mice; Fig. 1L, M). Furthermore, when assessing spontaneous behavior in the home-cage, we observed that KO mice displayed a marked increase in repetitive rearing episodes (Fig. 1N), further supporting the presence of stereotypic behavior (WT: 25.41 ± 2.317 vs. KO: 33.68 ± 2.236). Female KO mice exhibited hypersensitivity to tactile stimuli in Von Frey tests (Fig. 1O-Q). Approximately 33% of ASD patients have co-occurring intellectual disability [42]. Nevertheless, novel object recognition and Morris water maze tests showed no learning/memory deficits in KO mice (Fig. S2C-D). Collectively, *Sh3rf3* KO mice recapitulate core autistic-like behaviors, including social deficits, anxiety and repetitive/stereotyped behavior, and sensory abnormalities.

Sh3rf3 deficiency reduces excitatory synaptic strength in the prefrontal cortex

To determine the brain region underlying the ASD-like behavior, we inspected the *Sh3rf3* level in *Sh3rf3*+/- (heterozygote, HET) brain with LacZ antibody, as its first exon was replaced by β-galactosidase gene (Fig. S1B). Immunofluorescence and RT-PCR results revealed that *Sh3rf3* was broadly expressed both temporally and spatially, especially in excitatory neurons and some interneurons (Fig. S3A-D). Since the prefrontal cortex (PFC) regulates social behavior [43–47], we prioritized PFC for investigation. To test whether PFC-specific *Sh3rf3* knockdown induces autistic-like behavior, we delivered *Sh3rf3* shRNA AAV (GFP-tagged) bilaterally to the medial PFC of 4-week-old mice. The knockdown efficiency was confirmed by significantly reduced *Sh3rf3* mRNA levels (~70%; Fig. 2A). Three weeks post-injection, mice underwent the habituation-novelty recognition task. Knockdown mice exhibited significantly reduced interaction time with stranger mice and a lower social cognition index (WT: 18.5 ± 2.975 vs. KD: 2.782 ± 0.8448 s; Fig. 2B), indicating the social withdrawal of knockdown mice. However, knockdown of *Sh3rf3* specifically in
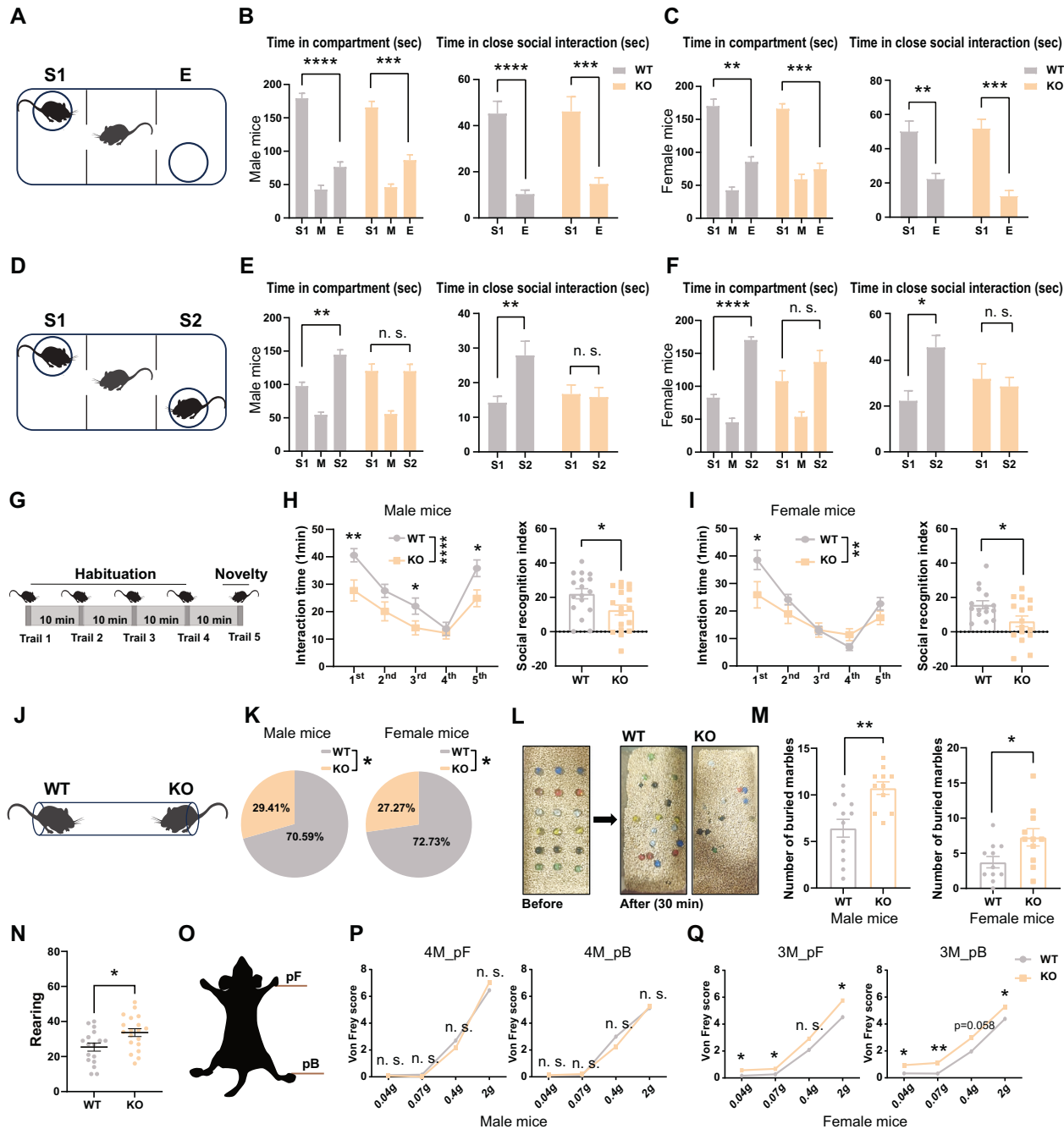
Fig. 1 ***Sh3rf3* deletion results in autistic-like phenotypes in mice. (A-C)** Three-chamber sociability test. Diagram of the test (A). Bar graphs showing the performance of male (B) or female mice (C), including the time spent in different chambers (Left), and the interaction time during the sociability test (Right). E, empty chamber; M, middle chamber; S1, stranger 1. n = 14 (WT), n = 15 (KO) for males and n = 10 (WT), n = 11 (KO) for females, two-way ANOVA. **(D-F)** Three-chamber social novelty test. Diagram of the test (D). Bar graphs showing the performance of male (E) or female mice (F), including the time spent in different chambers (Left), and the interaction time during the social novelty test (Right). S2: stranger 2. n = 14 (WT), n = 15 (KO) for males and n = 10 (WT), n = 11 (KO) for females, two-way ANOVA. **(G-I)** Habituation/novelty recognition task behavioral paradigm. Diagram of the test (G). Statistical graphs showing the performance of male (H) or female mice (I), including the social interaction time with stranger mice (Left), two-way ANOVA; and the social recognition index (Right), *t-test*. n = 17 (WT), n = 18 (KO) for males and n = 15 (WT); n = 16 (KO) for females. **(J)** Schematic diagram of the tube-dominance test. **(K)** Statistical graph of victory rates between male (Left) or female (Right) mice. WT and KO mice; n = 17 (WT), n = 17 (KO) for males and n = 11 (WT), n = 11 (KO) for females. Chi-square test. **(L)** Representative results in the marble burying test. **(M)** Bar graphs showing the buried marbles of male (Left) or female (Right) mice, *t-test*. n = 12 (WT), n = 11 (KO) for male mice and n = 11 (WT), n = 11 (KO) for female mice. **(N)** Bar graph of rearing episodes in the home-cage, *t-test*. n = 17 (WT), n = 19 (KO). **(O)** Diagram of mouse anatomy. pF: paws Front, pB: paws Behind. **(P, Q)** Statistical graphs of Von Frey scores for male (O) or female (P) mice. n = 12 paws/6 mice (WT), n = 12 paws/6 mice (KO) for males and n = 30 paws/15mice (WT), n = 28 paws/14 mice (KO) for females; two-way ANOVA.
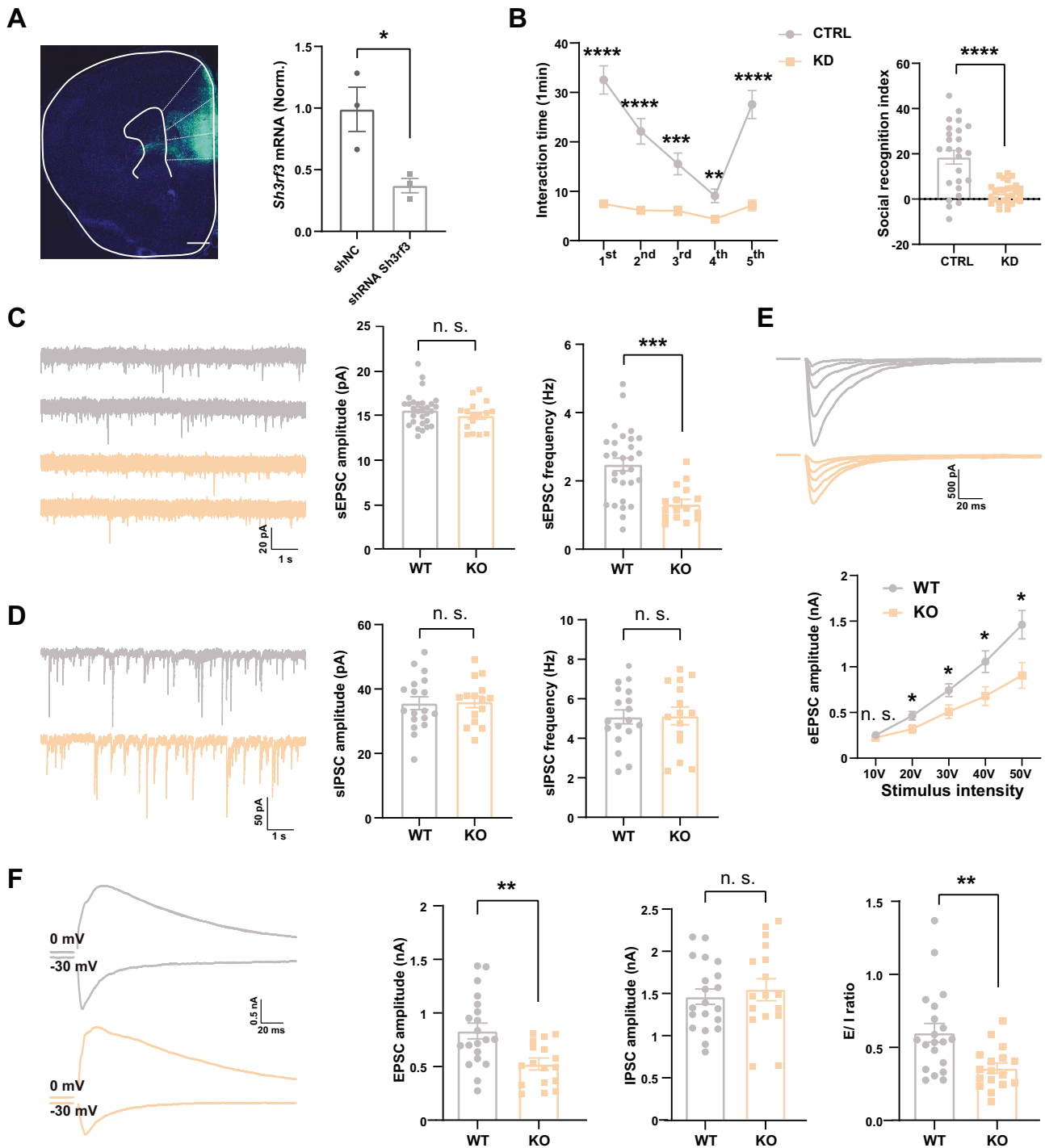
Fig. 2 *Sh3rf3* deficiency leads to a decline in excitatory synaptic transmission in PFC. (A) A confocal image showing the viral-infected PFC region (stained with DAPI) from a mouse with the stereotaxic injection of *Sh3rf3* shRNA AAV (GFP-tagged). Scale bar: 500 µm. Quantitative PCR data showing the *Sh3rf3* mRNA levels in PFC injected with *Sh3rf3* shRNA or scrambled (sc) shRNA. n = 3/group, *t-test*. **(B)** Statistical graphs of the social interaction time of control and *Sh3rf3* knockdown mice with the stranger mice; two-way ANOVA; and the social recognition index for male mice, n = 25 (Ctrl); n = 28 (KD), *t-test*. **(C)** Representative traces of sEPSCs recorded in the PFC in the presence of PTX (Left). Amplitude (Medium) and frequency (Right) of sEPSCs recorded in PFC layer 5 neurons. n = 29 neurons/5 mice (WT), n = 16 neurons/3 mice (KO), *t-test*. **(D)** Representative traces of sIPSCs recorded in the PFC in the presence of CNQX and D-APV (Left). Amplitude (Medium) and frequency (Right) of sIPSCs recorded in PFC layer 5 neurons. High-Cl intracellular pipette solution was used to record inward sIPSCs at holding potential of -70 mV. n = 18 neurons/3 mice (WT), n = 15 neurons/3 mice (KO), *t-test*. **(E)** Representative traces of evoked EPSCs recorded in the PFC in the presence of PTX (Up); and statistical graph of evoked EPSCs amplitudes (Down); n = 30 neurons/5 mice (WT), n = 17 neurons/3 mice (KO), two-way ANOVA. **(F)** Representative traces of EPSC (at holding potential of -30 mV) and IPSC (at holding potential of 0 mV) recorded from the same neuron; statistical graphs of evoked EPSC amplitudes and IPSC amplitudes and the EPSC/IPSC ratio; n = 20 neurons/4 mice (WT), n = 17 neurons/4 mice (KO). *t-test*.
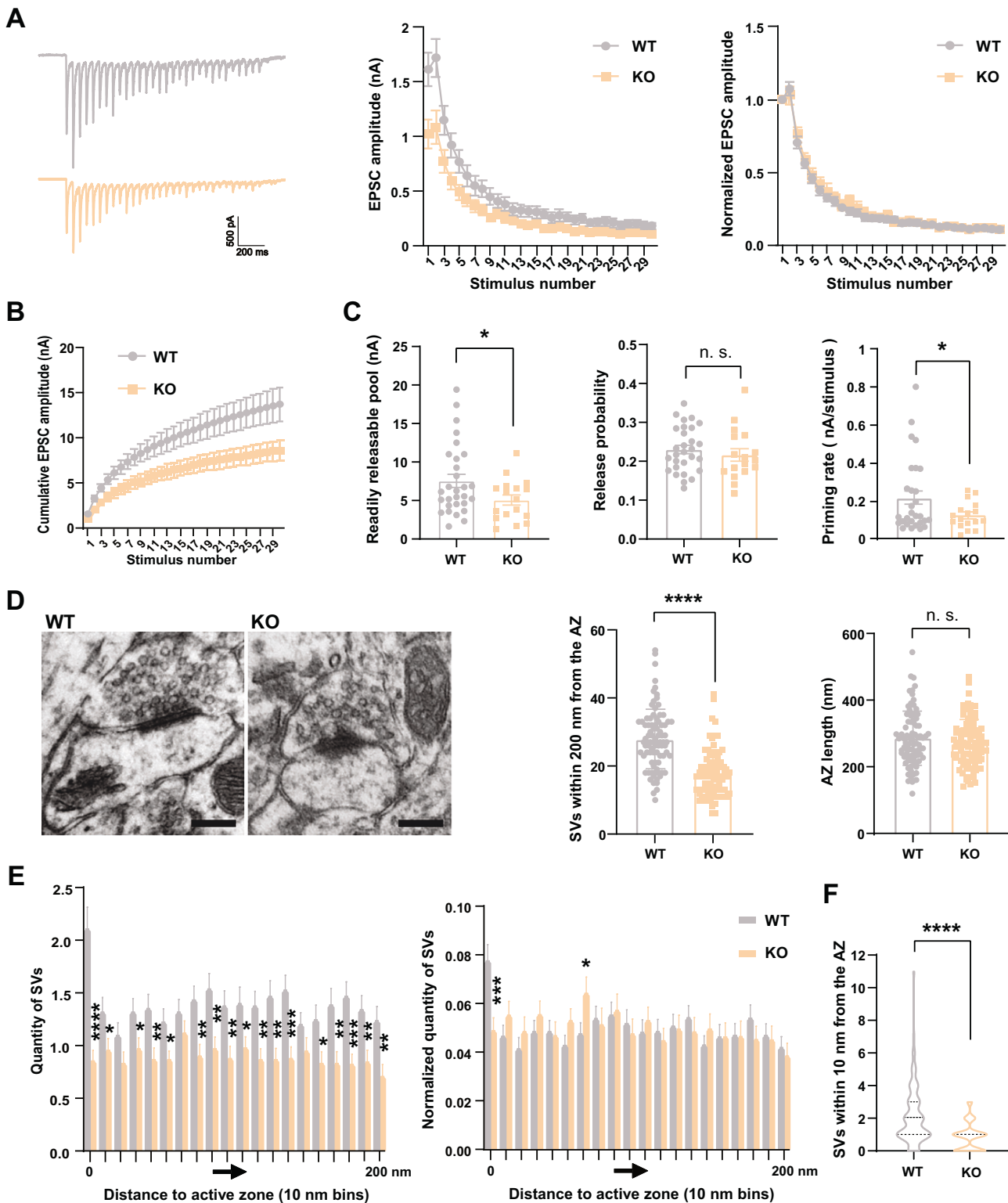
Fig. 3 The loss of *Sh3rf3* results in a decrease in RRP size and priming rate in the PFC. (A) Representative traces of EPSCs evoked by a train of fiber stimulation (20 Hz) in acute PFC slices from littermate WT and *Sh3rf3* KO mice at P42–P55 (Left). Statistical graph showing the amplitudes (Middle) and normalized amplitudes (Right) of EPSCs recorded during a train of stimulation. **(B)** Statistical graph showing the cumulative amplitudes of EPSCs recorded during train stimulation of the presynaptic terminal. **(C)** Statistical graphs of the readily releasable pool, release probability and priming rate. n = 29 neurons/3 mice (WT), n = 17 neurons/3 mice (KO), *t-test*. **(D)** Representative transmission electron microscopy (TEM) micrographs of the PFC, scale bar, 200 nm. Statistical graphs showing the synaptic vesicles (SVs) within 200 nm from the active zone and length of the active zone (AZ) in the PFC. n = 86 profiles/5 mice (WT), n = 88 profiles/5 mice (KO), *t-test*. **(E)** Quantity of SVs within different distances from AZ and normalized quantity of SVs within 200 nm from the AZ in the PFC. n = 86 profiles/5 mice (WT), n = 88 profiles/5 mice (KO), Mann-Whitney test. **(F)** Statistical graph of SVs within 10 nm from the active zone in the PFC. n = 86 profiles/5 mice (WT), n = 88 profiles/5 mice (KO), *t-test*.
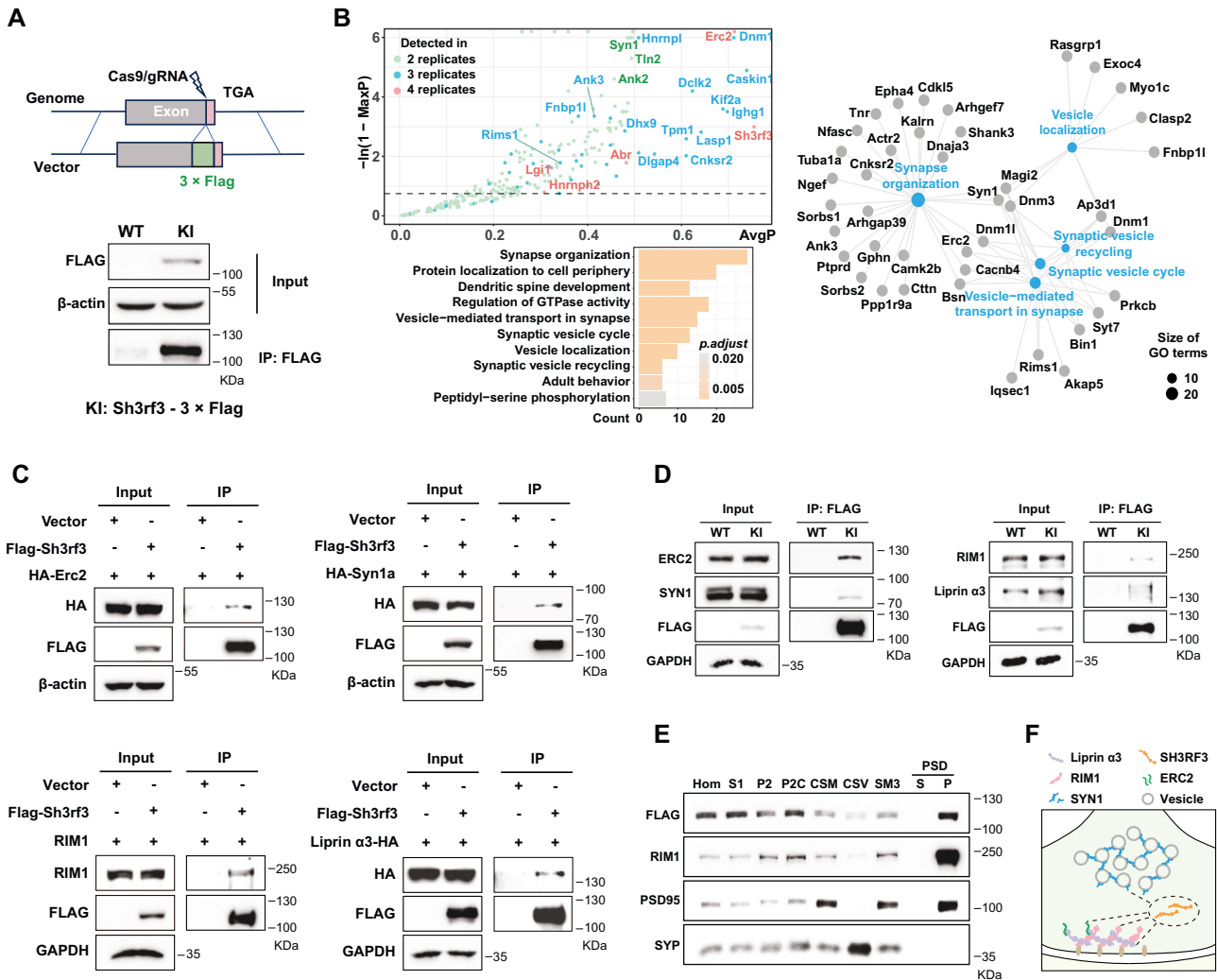
Fig. 4 SH3RF3 interacts with presynaptic proteins. (A) Schematic representation of the construction strategy for *Sh3rf3-3 × flag* mice (Top), Enrichment of adult WT and *Sh3rf3-3 × flag* mouse PFC tissue samples using FLAG beads (Bottom). **(B)** Analysis of IP-MS data. Dot graph showing the binding probabilities of prey proteins, with a dashed line indicating the threshold of MaxP = 0.5 (Left-top). Bar graph showing the GO-BP enrichment terms of repeatedly detected prey proteins with MaxP > 0.5 (Left-bottom). Network diagram of some significantly enriched GO-BP terms and proteins in them (Right). AvgP, average binding probability; MaxP, maximum binding probability. **(C)** Exogenous immunoprecipitation analysis demonstrated that SH3RF3 is capable of interacting with ERC2, Synapsin1, RIM1 and Liprin α3. **(D)** Interaction between SH3RF3 and presynaptic proteins ERC2, Synapsin1, RIM1 and liprin α3 was detected in mouse PFC. **(E)** Subcellular distribution. Mouse brain homogenates were subjected to subcellular fractionation, and an aliquot of each fraction (10 μg) was analyzed by western blotting with the indicated antibodies. The results are representative of three independent experiments. Hom, homogenate; S1, crude synaptosomal fraction; P2, crude membrane fraction; P2C, synaptosomal fraction; CSM, crude synaptic membrane fraction; CSV, crude SV fraction; SM3, synaptosomal membrane; PSD, postsynaptic density fraction; S, 1% (w/v) Triton X-100-soluble fraction of PSD; P, 1% Triton X-100-insoluble fraction of PSD. **(F)** Illustrative diagram of SH3RF3 interacting with presynaptic proteins.
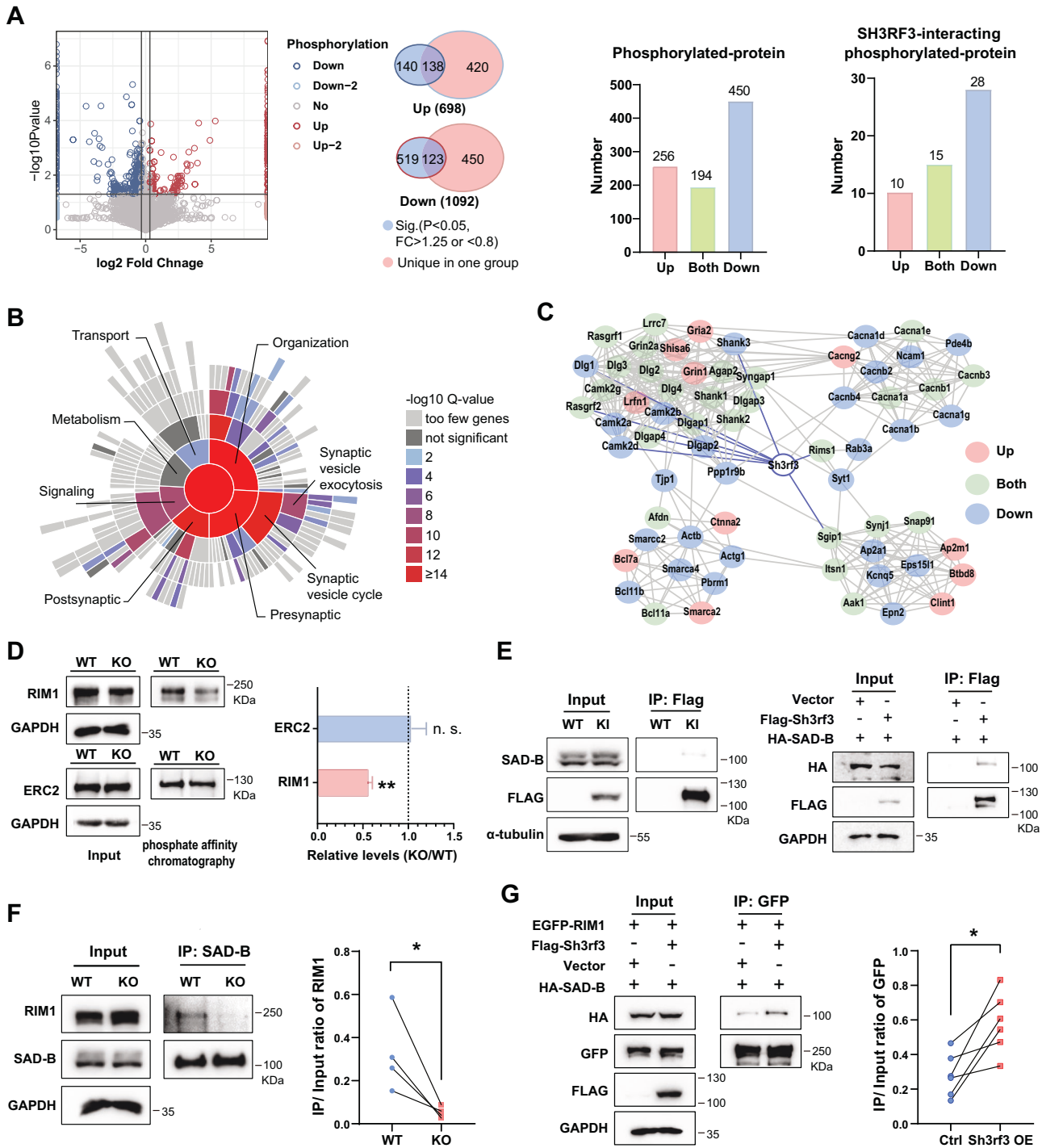
the mPFC does not induce anxiety-like or repetitive stereotyped behaviors in mice (Fig. S4A-D).

We next evaluated synaptic function in the PFC layer 5 pyramidal neurons using whole-cell patch-clamp recordings. Spontaneous excitatory postsynaptic current (sEPSC) frequency, but not amplitude, decreased significantly in KO mice (WT: 2.553 ± 0.1563 vs. KO: 1.334 ± 0.1288 Hz for frequency; Fig. 2C). Meanwhile, the amplitude of the evoked EPSC (eEPSC) significantly declined, while the amplitude and frequency of spontaneous inhibitory postsynaptic current (sIPSC) were unchanged (Fig. 2D, E). Consistently, recording EPSC and IPSC from the same neuron revealed significantly reduced EPSC amplitude but unchanged IPSC amplitude (WT: 0.8324 ± 0.07357 vs. KO: 0.5227 ± 0.04816 nA for EPSC amplitude; Fig. 2F), indicating the disruption of excitation/ inhibition (E/I) balance (WT: 0.6008 ± 0.06409 vs. KO: 0.3582 ± 0.03468; Fig. 2F). These results

suggest that *Sh3rf3* is required for normal excitatory synaptic function.

Sh3rf3 loss decreases the readily releasable vesicle pool and attenuates vesicle replenishment

To investigate the cause of defective excitatory synaptic transmission in PFC, we quantified the dendritic complexity and spine density in both WT and KO neurons. Sholl analysis of cortical pyramidal neurons cultured in vitro for 14 days showed no changes in the dendritic complexity (Fig. S5A). *Thy1-GFPm*-labeled PFC pyramidal neurons in KO mice displayed a trend toward reduced spine density (WT: 10.1 ± 0.4182 vs. KO: 9.108 ± 0.3136 per 10 μm) and no difference in spine subtypes (Fig. S5B). Consistently, excitatory (VGluT1 + , encoded by *Slc17a7*) or inhibitory (VGAT + , encoded by *Slc32a1*) synapse counts and ratios were unchanged (Fig. S5C). Neuronal excitability as a

A

B

C

D

E

F

G

measurement of neuronal firing frequency, and the total protein levels and phosphorylation levels of the AMPA receptor subunits were unaffected (Fig. S6A, B). Consistently, miniature EPSC (mEPSC) amplitudes were normal (Fig. S6C), suggesting post-synaptic function is not affected in KO neurons.

We went on to inspect the presynaptic function in PFC using paired-pulse ratio (PPR) of various inter-stimulus intervals (ISIs) and found no significant differences (Fig. S6D). However, high-frequency stimulation revealed a smaller size of the readily releasable pool (RRP) (WT: 7.547 ± 0.85 vs. KO: 5.069 ± 0.6591 nA) and slower replenishment rate (WT: 0.2412 ± 0.04265 vs. KO:

0.1243 ± 0.01693 nA/stimulus) in KO mice, with no change in release probability (Fig. 3A-C), implicating the disturbance of synaptic vesicle distribution. Through transmission electron microscope (TEM), we observed that significantly changed distribution and decreased number of synaptic vesicles within 200 nm from the presynaptic active zone (AZ) in KO terminals (WT: 27.90 ± 0.9515 vs. KO: 17.95 ± 0.7287), particularly within 10 nm (WT: 2.116 ± 0.1981 vs. KO: 0.8636 ± 0.09169), despite normal AZ length (Fig. 3D-F). These results suggest that *Sh3rf3* loss alters synaptic vesicle distribution, impairing the excitatory transmission.

Fig. 5 **The loss of *Sh3rf3* diminishes the phosphorylation of RIM1 by SAD-B/BRSK1. (A)** Volcano plot for differential analysis of quantitative protein phosphorylation profiling of mouse PFC (Left); statistical graphs of the number of proteins with altered phosphorylation levels (Middle) and SH3RF3-interacting proteins with altered phosphorylation levels (Right). Dashed lines represent the FC > 1.25 or FC < 0.8 and *p-value* threshold of 0.05. FC, fold change. n = 3 replicates per condition. **(B)** Sunburst plot representing biological process enrichment results of changed phosphorylated proteins by *Sh3rf3* deficiency. Higher red intensities are associated with more significant enrichments. **(C)** A protein interaction network diagram was constructed by combining the results of SH3RF3 immunoprecipitation mass spectrometry and quantitative phosphorylation mass spectrometry analysis. Blue lines indicate interactions confirmed by interaction mass spectrometry, while gray lines represent predicted or previously reported interactions. Red circles signify an upregulation of phosphorylation levels, blue circles indicate a downregulation of phosphorylation levels, and green circles represent both upregulation and downregulation of phosphorylation levels simultaneously. **(D)** Overall phosphorylation levels of RIM1 and ERC2 in PFC. Total protein and enriched phosphorylation levels (Left) and statistical graph of phosphorylation levels of RIM1 and ERC2 (Right); n = 4 (WT), n = 4 (KO), *t-test*. **(E)** Interaction between SH3RF3 and BRSK1 in mouse PFC (Left); Exogenous immunoprecipitation demonstrated that SH3RF3 is capable of interacting with BRSK1 (Right). **(F)** The interaction between RIM1 and BRSK1 inspected in the PFC of WT and KO mice. A statistical graph showing the ratio of gray values between IP samples and their corresponding Input samples, n = 4 (WT), n = 4 (KO), *t-test*. **(G)** Expression of SH3RF3, RIM1, and BRSK1 in HEK293 cells to examine the effect of SH3RF3 on the interaction between RIM1 and BRSK1 (Left). Statistical graph of the grayscale value ratio of IP samples to corresponding input samples, n = 6 (Ctrl), n = 6 (*Sh3rf3* OE) (Right), *t-test*, Ctrl: control, OE: over-expression.

Newly identified SH3RF3-interacting proteins indicate presynaptic roles

To delve into the underlying mechanisms for impaired excitatory transmission, we performed immunoprecipitation mass spectrometry (IP-MS) in *Sh3rf3-3×flag* knock-in mice and identified 167 potential SH3RF3-interacting proteins, 22% of which are associated with ASD based on SFARI database [48] (Fig. 4A, Fig. S7A, B, Table S5). Gene Ontology analysis of proteins that interacted with SH3RF3 indicated that they were highly associated with synaptic transmission and vesicle recycling (Fig. 4B). We uncovered intriguing interactions between SH3RF3 and a cohort of presynaptic active zone proteins, namely RIM1, Liprin-α3, ERC2, and Synapsin1 and confirmed that by both endogenous and exogenous co-IP experiments (Fig. 4C, D). Notably, RIM1, Liprin-α3, and ERC2 serve as pivotal components within the presynaptic AZ [18, 49, 50].

Our above findings indicate SH3RF3's important role in the presynaptic landscape (Fig. 4F). We performed western blot analysis of PFC subcellular fractionations and confirmed the SH3RF3's presynaptic localization, colocalizing with RIM1 in crude synaptic membrane (CSM) fraction, and with synaptic vesicle marker SYN in crude synaptic vesicle (CSV) fraction (Fig. 4E). This cumulative evidence highlighted the presynaptic localization and function of SH3RF3.

Sh3rf3 KO attenuates the phosphorylation of RIM1 by BRSK1/SAD-B

The functions of presynaptic active zone proteins are highly dependent on phosphorylation [24, 51–53]. Since our IP-MS results indicate that SH3RF3 interacts with specific protein kinases and phosphatases, we conducted both 6Plex-tandem mass tag (TMT)-labeled quantitative proteomics and phosphoproteomic assays in WT and KO PFC (Table S6, 7). The 6Plex-TMT and western blot analyses revealed unchanged overall expression of SH3RF3-interacting proteins (Fig. S7A-C), whereas the phosphorylation levels of 900 proteins were altered, including 53 SH3RF3-interacting proteins (Fig. 5A). SynGO analysis on the differentially expressed phosphoproteins indicated the preferentially enriched GO term in synaptic organization and process in the presynaptic functions, especially synaptic vesicle cycle and synaptic vesicle exocytosis (Fig. 5B). Of note, the significant changes in the phosphorylation of newly identified SH3RF3-interacting protein RIM1, in KO mice (Fig. 5C), implicating the role of SH3RF3 in regulating synaptic function via protein phosphorylation.

To further validate this finding, we employed a phos-tag-based magnetic-bead method to rapidly and selectively enrich phosphorylated proteins. This revealed a ~50% reduction in RIM1 phosphorylation levels in KO PFC, while ERC2 remained unchanged (Fig. 5D). This suggests that *Sh3rf3* KO reduces RIM1 phosphorylation, potentially impacting presynaptic vesicle number and distribution. To explore the mechanism, we focused on kinases known to phosphorylate RIM1: BRSK1/SAD-B, PKA, and SRPK2 [22, 52, 53]. Reviewing our SH3RF3 IP-MS data, we identified potential interactions with BRSK1 and SRPK2 (Table S5). Subsequent exogenous and endogenous co-IP experiments confirmed that SH3RF3 interacts with BRSK1/SAD-B, but not SRPK2 or PKA (Fig. 5E).

BRSK1/SAD-B, a presynaptic serine/threonine kinase regulating the releasable vesicle pool, can phosphorylate RIM1 in vitro [22]. Given that SH3RF3 interacts with both RIM1 and BRSK1, we hypothesized that SH3RF3 facilitates the phosphorylation of RIM1 by BRSK1. Examining BRSK1-RIM1 interaction in WT and KO PFC, we found a significant reduction (~80%) in their association in KO tissue (Fig. 5F). Conversely, *Sh3rf3* overexpression significantly enhanced this interaction (~200%) in HEK293 cells (Fig. 5G). Together, these data demonstrate that SH3RF3 acts as a scaffold protein to mediate BRSK1-dependent phosphorylation of RIM1.

Re-expression of *Sh3rf3* in PFC can rescue the social and functional deficits in *Sh3rf3* KO mice

Significantly reduced RIM1 phosphorylation in KO mice may result in a marked decrease in vesicles docked at the active zone, causing E/I imbalance and autistic-like behaviors in mice. To determine whether *Sh3rf3* re-expression could rescue social dysfunction in KO mice, we injected *Sh3rf3*-overexpressing virus (AAV-hSyn-EGFP-P2A-Sh3rf3-tWPA) and control virus into the PFC of WT or KO mice. Three weeks post-injection, qPCR analysis showed that following *Sh3rf3*-overexpressing virus injection, *Sh3rf3* mRNA increased in both WT and KO mice, reaching similar high expression levels. (Fig. 6A).

We evaluated social behavior using a habituation-novelty recognition task across four groups: WT and KO mice injected with the control virus, and WT and KO mice injected with the *Sh3rf3*-overexpressing virus. KO mice injected with control virus showed significantly shorter social interaction time with stranger mice than other groups (Fig. 6B). In contrast, *Sh3rf3* re-expression in KO mice restored social interaction time to levels similar to controls, with consistent results in social recognition index (Fig. 6B). Furthermore, overexpression of *Sh3rf3* significantly increased the frequency of sEPSCs in KO mice, while having minimal effect on their amplitude (Fig. 6C). Moreover, it significantly enhanced RIM1 phosphorylation, restoring it to levels comparable to those in controls (Fig. 6D). These findings indicate that *Sh3rf3* re-expression can rescue social and functional deficits in KO mice and underscores its essential role in maintaining PFC function.

DISCUSSION

The pathogenic mechanisms underlying ASD exhibit considerable heterogeneity across diverse genetic contributors. Elucidating
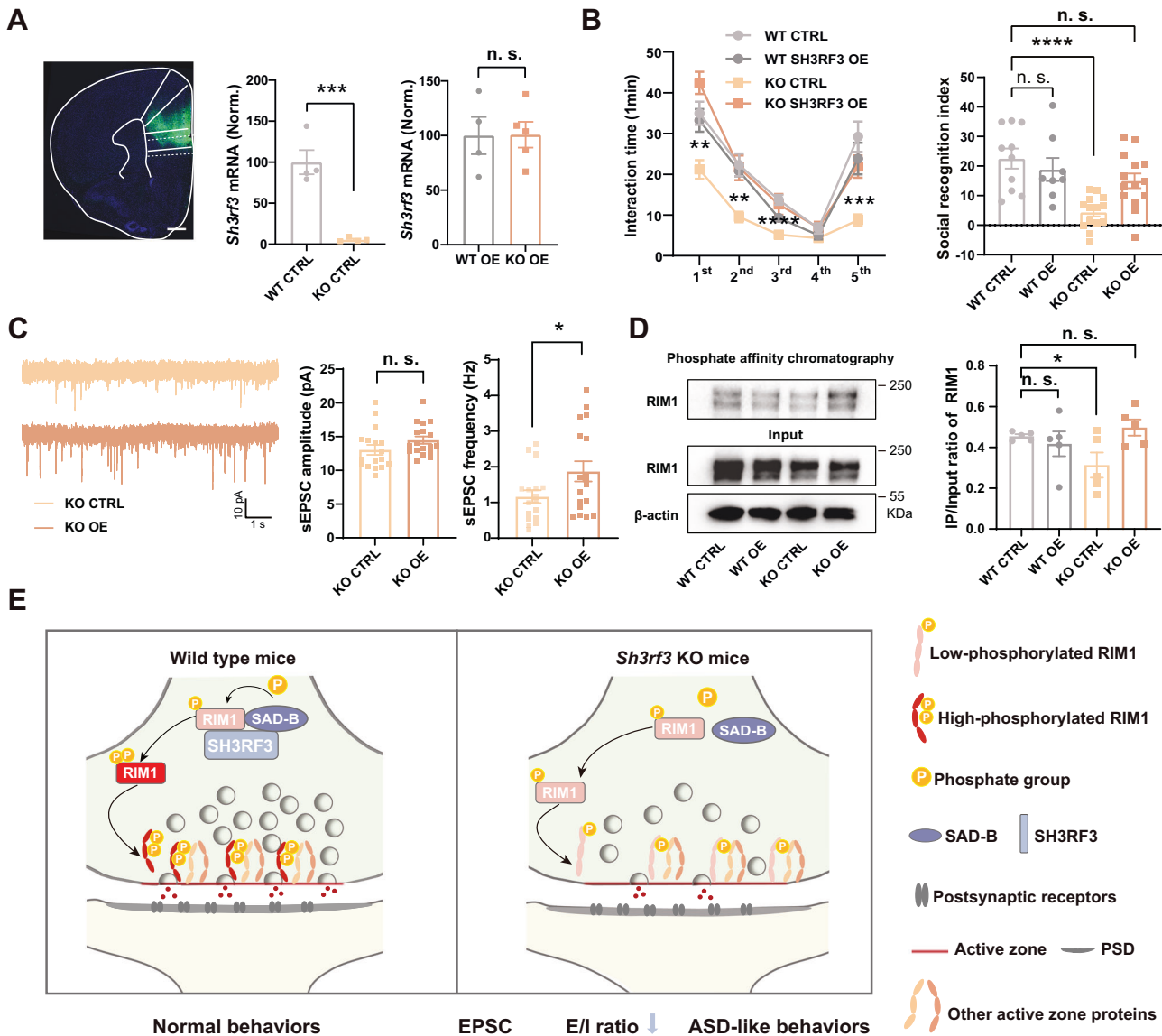
Fig. 6 *Sh3rf3* re-expression in the PFC of *Sh3rf3* KO mice can rescue their social and functional deficits. **(A)** A confocal image showing the viral-infected PFC region (stained with DAPI, blue) from a mouse with the stereotaxic injection of *Sh3rf3* overexpression AAV (GFP-tagged). Scale bar: 500 μm. Quantitative PCR data showing *Sh3rf3* mRNA levels in PFCs injected with *Sh3rf3* overexpression or control virus. n = 4/group, *t-test*. **(B)** Statistical graphs of the social interaction time of subject mice with the stranger mice; two-way ANOVA; and the social recognition index for male mice, one-way ANOVA, n = 10 (WT CTRL); n = 8 (WT OE); n = 14 (KO CTRL); n = 14 (KO OE). CTRL: control, OE: overexpression. **(C)** Representative traces of sEPSCs recorded in the PFC in the presence of PTX (Left). Amplitude (Medium) and frequency (Right) of sEPSCs recorded in PFC layer 5 neurons. n = 17 neurons/4 mice (KO CTRL), n = 18 neurons/4 mice (KO OE), *t-test*. **(D)** Overall phosphorylation levels of RIM1 in PFC. Total protein and enriched phosphorylation levels (Left) and statistical graph of phosphorylation levels of RIM1 (Right); n = 5/group, *t-test*. **(E)** At the pre-synapses, SH3RF3 serves as a scaffold protein, mediating the interaction between serine/threonine protein kinase BRSK1 and the constitutive core protein RIM1 in the active zone, thereby regulating the phosphorylation of RIM1. The absence of SH3RF3 results in a reduced interaction between BRSK1 and RIM1, leading to the reduced phosphorylation of RIM1. This impacts the docking of vesicles to the presynaptic membrane, reduces excitatory presynaptic synaptic transmission, disrupts the E/I balance, and ultimately leads to autism-like behaviors in mice.

genotype-specific pathophysiological mechanisms would facilitate a holistic understanding of ASD etiology, laying the groundwork for novel therapeutic strategies. Our study demonstrates the causal link between the deficiency of SH3RF3 and autistic-like phenotypes in mice. Using multimodal analyses including electron microscopy, electrophysiology, quantitative proteomics, and phosphoproteomics, we identify SH3RF3 as a novel molecular scaffold that bridges ASD-risk components, connecting BRSK1/SAD-B kinase activity to active zone machinery (via RIM1 phosphorylation) to regulate vesicle dynamics (Fig. 6E).

Social cognition emerges from distributed neural networks incorporating cortical regions (e.g., mPFC, anterior cingulate cortex, and insular cortex) and subcortical nuclei (e.g., nucleus accumbens, basolateral amygdala, and ventral tegmental area), modulated by diverse neuromodulatory systems [54]. The mPFC serves as a critical integration hub, coordinating cross-regional information flow to regulate social-emotional processing, decision-making, and mnemonic functions [54–56]. Although SH3RF3 demonstrates pan-cerebral expression, its specific knockdown in the mPFC significantly reduces social interaction time, and

mPFC-specific re-expression rescues the social deficits in KO mice, underscoring its regionally pivotal role.

The excitatory/inhibitory (E/I) imbalance constitutes a characteristic neurobiological feature of ASD [57]. In our mouse model, we observed a reduction in the E/I ratio in the prefrontal cortex. Reduction in oscillatory power within the low-gamma frequency range in *Sh3rf3* KO mice was also observed by in vivo electrophysiological recordings of mPFC (Fig. S8A, B), further suggesting the disruption of E/I balance. This finding aligns with some autism mouse models [12, 13, 58], although others show an increased E/I ratio [59, 60]. While synaptic dysfunction frequently mediates this imbalance, conventional paradigms typically implicate postsynaptic alterations such as aberrant mEPSC amplitude or inhibitory transmission [12, 13]. Notably, our *Sh3rf3* KO mice exhibit unchanged mEPSC amplitude and intact postsynaptic ultrastructure, including unaltered dendritic arborization, spine density, and glutamatergic/GABAergic synaptic puncta, distinguishing it from canonical ASD models with postsynaptic pathophysiology. Alterations in presynaptic function can also contribute to ASD, though most of the evidence reflects changes in excitability or the number of synapses [8, 61–63]. Only a few of them identified impaired vesicle recycling as the trigger of ASD [64, 65]. Our investigation reveals a novel presynaptic etiology: diminished readily releasable vesicle pool size specifically compromises excitatory neurotransmission, thereby reducing the E/I ratio. This discovery elucidates a previously underappreciated presynaptic contribution to ASD pathophysiology, establishing vesicle dynamics regulation as a critical mechanism in E/I imbalance. The distinct presynaptic pathology observed in our model provides unique insights into the mechanistic diversity underlying ASD-related synaptic dysfunctions.

SH3RF3 has been previously identified as an E3 ubiquitin ligase, but our KO mice showed no significant changes in presynaptic protein levels, nor did it affect the ubiquitination of its interacting proteins, including BRSK1 and RIM1 (Fig. S7D, E). Thus, its function as a scaffold protein appears to play a dominant role in the KO mouse phenotype. Mechanistically, we identified 167 SH3RF3-interacting proteins, 22% of which are associated with ASD based on the SFARI database [48]. These include presynaptic regulators of cytoskeleton (ANK2 and TRIO) [66, 67], cell adhesion and signaling (CTNND1 and PTPRD) [68, 69], local mRNA translation (SYNCRIP) [70], and neurotransmitter release (RIM1 and SYN1) (Fig. S9A, B) [17, 71]. As a scaffold protein, SH3RF3 may form distinct complexes across brain regions, positioning it as a synaptic hub in the ASD-risk network. Omics analysis revealed minimal changes in protein expression but significant phosphorylation state alterations, suggesting SH3RF3 as an important phosphorylation regulator. We confirmed SH3RF3's interaction with both BRSK1/SAD-B and ASD-associated active zone protein RIM1, and its role in RIM1 phosphorylation. RIM1 is well established to regulate synaptic vesicle priming and tether presynaptic voltage-gated calcium channels (VGCCs) to vesicles [18]. The decreased colocalization between $Ca_v2.1$ and the synaptic vesicle protein VGluT1 (Fig. S10A, B) further supports RIM1 dysfunction caused by the KO of *Sh3rf3*. The decrease in synaptic vesicles adjacent to VGCCs suggests impaired vesicle docking/priming, which is consistent with the results of electrophysiology (Fig. 4A-C) and electron microscopy (Fig. 4D-F) and further links SH3RF3 loss to impaired excitatory transmission. Besides, a previous study had identified human RIM1 aa1135-1206 as the potential target of SAD-B, and this region is correlated to RIM1 aa906-977 in mouse [22], which might be the target region of mouse SAD-B.

Our study provides a comprehensive framework linking *Sh3rf3* loss to autistic-like behaviors through behavioral, synaptic, and molecular mechanisms. While *Sh3rf3* is widely expressed, we hypothesize region- and developmental stage-specific roles. Future work should explore its functions in other social-behavior circuits (e.g., nucleus accumbens, amygdala) and their circuit-level interactions. Whether additional pathways contribute to autistic behaviors warrants further investigation.

In summary, this study establishes SH3RF3 as a critical regulator of presynaptic function in the mPFC, linking its loss to autism-like behaviors via disrupted BRSK1/RIM1 signaling and vesicle dynamics. Departing from the field's conventional focus on postsynaptic mechanisms, the work uncovers a presynaptic origin of excitatory/inhibitory (E/I) imbalance and proposes innovative therapeutic strategies targeting synaptic vesicle release pathways to restore neuronal communication.

DATA AVAILABILITY

REFERENCES

1. Li CX, He WQ. Prevalence and treatment of autism spectrum disorder in the United States, 2016-2022. Autism Research. 2024;17:1916–27.
2. Abrahams BS, Geschwind DH. Advances in autism genetics: on the threshold of a new neurobiology. Nat Rev Genet. 2008;9:341–55.
3. Bourgeron T. From the genetic architecture to synaptic plasticity in autism spectrum disorder. Nat Rev Neurosci. 2015;16:551–63.
4. Satterstrom FK, Kosmicki JA, Wang JB, Breen MS, De Rubeis S, An JY, et al. Large-scale exome sequencing study implicates both developmental and functional changes in the neurobiology of autism. Cell. 2020;180:568–84.
5. Lu H, Zuo L, Roddick KM, Zhang P, Oku S, Garden J, et al. Alternative splicing and heparan sulfation converge on neurexin-1 to control glutamatergic transmission and autism-related behaviors. Cell Reports. 2023;42:112714.
6. Peça J, Feliciano C, Ting JT, Wang WT, Wells MF, Venkatraman TN, et al. Shank3 mutant mice display autistic-like behaviours and striatal dysfunction. Nature. 2011;472:437–42.
7. Schmeisser MJ, Ey E, Wegener S, Bockmann J, Stempel AV, Kuebler A, et al. Autistic-like behaviours and hyperactivity in mice lacking ProSAP1/Shank2. Nature. 2012;486:256–60.
8. Spratt PWE, Ben-Shalom R, Keeshen CM, Burke KJ, Clarkson RL, Sanders SJ, et al. The autism-associated gene Scn2a contributes to dendritic excitability and synaptic function in prefrontal cortex. Neuron. 2019;103:673–85.
9. Tabuchi K, Blundell J, Etherton MR, Hammer RE, Liu X, Powell CM, et al. A Neuroligin-3 mutation implicated in autism increases inhibitory synaptic transmission in mice. Science. 2007;318:71–76.
10. Delorme R, Ey E, Toro R, Leboyer M, Gillberg C, Bourgeron T. Progress toward treatments for synaptic defects in autism. Nat Med. 2013;19:685–94.
11. Chao HT, Chen HM, Samaco RC, Xue MS, Chahrour M, Yoo J, et al. Dysfunction in GABA signalling mediates autism-like stereotypies and Rett syndrome phenotypes. Nature. 2010;468:263–9.
12. Sacai H, Sakoori K, Konno K, Nagahama K, Suzuki H, Watanabe T, et al. Autism spectrum disorder-like behavior caused by reduced excitatory synaptic transmission in pyramidal neurons of mouse prefrontal cortex. Nat Commun. 2020;11:5140.
13. Zhang K, Yu F, Zhu J, Han S, Chen JH, Wu XY, et al. Imbalance of excitatory/inhibitory neuron differentiation in neurodevelopmental disorders with an NR2F1 point mutation. Cell Reports. 2020;31:107521.
14. Südhof TC. The synaptic vesicle cycle: a cascade of protein-protein interactions. Nature. 1995;375:645–53.
15. Emperador-Melero J, Kaeser PS. Assembly of the presynaptic active zone. Curr Opin Neurobiol. 2020;63:95–103.
16. Südhof TC. The presynaptic active zone. Neuron. 2012;75:11–25.
17. Deng L, Kaeser PS, Xu W, Südhof TC. RIM proteins activate vesicle priming by reversing autoinhibitory homodimerization of Munc13. Neuron. 2011;69:317–31.
18. Han YY, Kaeser PS, Südhof TC Schneggenburger R. RIM determines Ca2+ channel density and vesicle docking at the presynaptic active zone. Neuron. 2011;69:304–16.

19. Kaeser PS, Deng L, Wang Y, Dulubova I, Liu X, Rizo J, et al. RIM proteins tether Ca2+ -channels to presynaptic active zones via a direct PDZ-domain interaction. Cell. 2011;144:282–95.

20. Schoch S, Castillo PE, Jo T, Mukherjee K, Geppert M, Wang Y, et al. RIM1α forms a protein scaffold for regulating neurotransmitter release at the active zone. Nature. 2002;415:321–6.

21. Schoch S, Mittelstaedt T, Kaeser PS, Padgett D, Feldmann N, Chevaleyre V, et al. Redundant functions of RIM1α and RIM2α in Ca2+-triggered neurotransmitter release. EMBO J. 2006;25:5852–63.

22. Inoue E, Mochida S, Takagi H, Higa S, Deguchi-Tawarada M, Takao-Rikitsu E, et al. SAD: A presynaptic kinase associated with synaptic vesicles and the active zone cytomatrix that regulates neurotransmitter release. Neuron. 2006;50:261–75.

23. McDonald NA, Tao L, Dong M-Q, Shen K. SAD-1 kinase controls presynaptic phase separation by relieving SYD-2/Liprin-α autoinhibition. PLoS Biol. 2023;21:e3002421.

24. Mochida S, Hida Y, Tanifuji S, Hagiwara A, Hamada S, Abe M, et al. SAD-B phosphorylation of CAST controls active zone vesicle recycling for synaptic depression. Cell Reports. 2016;16:2901–13.

25. Kärkkäinen S, Hiipakka M, Wang JH, Kleino I, Vähä-Jaakkola M, Renkema GH, et al. Identification of preferred protein interactions by phage-display of the human Src homology-3 proteome. EMBO Rep. 2006;7:186–91.

26. Kärkkäinen S, van der Linden M, Renkema GH. POSH2 is a RING finger E3 ligase with Rac1 binding activity through a partial CRIB domain. FEBS Lett. 2010;584:3867–72.

27. Yao MH, Meng MZ, Yang XY, Wang S, Zhang HS, Zhang F, et al. POSH regulates assembly of the NMDAR/PSD-95/Shank complex and synaptic function. Cell Reports. 2022;39:110642.

28. Wang S, Tan N, Zhu X, Yao M, Wang Y, Zhang X, et al. Sh3rf2 haploinsufficiency leads to unilateral neuronal development deficits and autistic-like behaviors in mice. Cell Rep. 2018;25:2963–71.

29. Chang SH, Liu JJ, Zhao YL, Pang T, Zheng XY, Song ZR, et al. Whole-genome sequencing identifies novel genes for autism in Chinese trios. Sci China Life Sci. 2024;67:2368–81.

30. Feliciano P, Zhou XY, Astrovskaya I, Turner TN, Wang TY, Brueggeman L, et al. Exome sequencing of 457 autism families recruited online provides evidence for autism risk genes. NPJ Genom Med. 2019;4:19.

31. Iossifov I, O'Roak BJ, Sanders SJ, Ronemus M, Krumm N, Levy D, et al. The contribution of coding mutations to autism spectrum disorder. Nature. 2014;515:216–21.

32. Suzuki T, Suzuki T, Raveau M, Miyake N, Sudo G, Tsurusaki Y, et al. A recurrent PJA1 variant in trigonocephaly and neurodevelopmental disorders. Ann Clin Transl Neurol. 2020;7:1117–31.

33. Ohtsuka T, Takao-Rikitsu E, Inoue E, Inoue M, Takeuchi M, Matsubara K, et al. Cast: a novel protein of the cytomatrix at the active zone of synapses that forms a ternary complex with RIM1 and Munc13-1. J Cell Biol. 2002;158:577–90.

34. Koopmans F, van Nierop P, Andres-Alonso M, Bymes A, Cijsouw T, Coba MP, et al. SynGO: an evidence-based, expert-curated knowledge base for the synapse. Neuron. 2019;103:217.

35. Tsunehiro M, Meki Y, Matsuoka K, Kinoshita-Kikuta E, Kinoshita E, Koike T. A Phos-tag-based magnetic-bead method for rapid and selective separation of phosphorylated biomolecules. Journal of Chromatography B. 2013;925:86–94.

36. Zhang N, Lin R, Gao W, Xu H, Li Y, Huang X, et al. Curcumin modulates PTPRZ1 activity and RNA m6A modifications in neuroinflammation-associated microglial response. Adv Sci. 2025;12:e2405263.

37. Xing M, Li Y, Zhang Y, Zhou J, Ma D, Zhang M, et al. Paraventricular hypothalamic RUVBL2 neurons suppress appetite by enhancing excitatory synaptic transmission in distinct neurocircuits. Nat Commun. 2024;15:8939.

38. Wang X, Cui X, Li Y, Li F, Li Y, Dai J, et al. MC4R deficiency causes dysregulation of postsynaptic excitatory synaptic transmission as a crucial culprit for obesity. Diabetes. 2022;71:2331–43.

39. Qin L, Williams JB, Tan T, Liu T, Cao Q, Ma K, et al. Deficiency of autism risk factor ASH1L in prefrontal cortex induces epigenetic aberrations and seizures. Nat Commun. 2021;12:6589.

40. Hörnberg H, Pérez-Garci E, Schreiner D, Hatstatt-Burklé L, Magara F, Baudouin S, et al. Rescue of oxytocin response and social behaviour in a mouse model of autism. Nature. 2020;584:252–6.

41. Fan Z, Zhu H, Zhou T, Wang S, Wu Y, Hu H. Using the tube test to measure social hierarchy in mice. Nat Protoc. 2019;14:819–31.

42. Zeidan J, Fombonne E, Scorah J, Ibrahim A, Durkin MS, Saxena S, et al. Global prevalence of autism: A systematic review update. Autism Research. 2022;15:778–90.

43. Amodio DM, Frith CD. Meeting of minds: the medial frontal cortex and social cognition. Nat Rev Neurosci. 2006;7:268–77.

44. Assaf M, Jagannathan K, Calhoun VD, Miller L, Stevens MC, Sahl R, et al. Abnormal functional connectivity of default mode sub-networks in autism spectrum disorder patients. Neuroimage. 2010;53:247–56.

45. Bickart KC, Hollenbeck MC, Barrett LF, Dickerson BC. Intrinsic amygdala–cortical functional connectivity predicts social network size in humans. J Neurosci. 2012;32:14729–41.

46. Sumiya M, Okamoto Y, Koike T, Tanigawa T, Okazawa H, Kosaka H, et al. Attenuated activation of the anterior rostral medial prefrontal cortex on self-relevant social reward processing in individuals with autism spectrum disorder. Neuroimage-Clin. 2020;26:102249.

47. Voineagu I, Wang XC, Johnston P, Lowe JK, Tian Y, Horvath S, et al. Transcriptomic analysis of autistic brain reveals convergent molecular pathology. Nature. 2011;474:380–4.

48. Abrahams BS, Arking DE, Campbell DB, Mefford HC, Morrow EM, Weiss LA, et al. SFARI Gene 2.0: a community-driven knowledgebase for the autism spectrum disorders (ASDs). Mol Autism. 2013;4:36.

49. Held RGLC, Kaeser PS. ELKS controls the pool of readily releasable vesicles at excitatory synapses through its N-terminal coiled-coil domains. eLife. 2016;5:e14862.

50. Wong MY, Liu C, Wang SSH, Roquas ACF, Fowler SC, Kaeser PS. Liprin-α3 controls vesicle docking and exocytosis at the active zone of hippocampal synapses. Proceedings of the National Academy of Sciences. 2018;115:2234–9.

51. Emperador-Melero J, Wong MY, Wang SSH, de Nola G, Nyitrai H, Kirchhausen T, et al. PKC-phosphorylation of Liprin-α3 triggers phase separation and controls presynaptic active zone structure. Nat Commun. 2021;12:3057.

52. Kaeser PS, Kwon HB, Blundell J, Chevaleyre V, Morishita W, Malenka RC, et al. RIM1alpha phosphorylation at serine-413 by protein kinase A is not required for presynaptic long-term plasticity or learning. Proc Natl Acad Sci USA. 2008;105:14680–5.

53. Müller JA, Betzin J, Santos-Tejedor J, Mayer A, Oprişoreanu A-M, Engholm-Keller K, et al. A presynaptic phosphosignaling hub for lasting homeostatic plasticity. Cell Reports. 2022;39:110696.

54. Sato M, Nakai N, Fujima S, Choe KY, Takumi T. Social circuits and their dysfunction in autism spectrum disorder. Mol Psychiatry. 2023;28:3194–206.

55. Anastasiades PG, Carter AG. Circuit organization of the rodent medial prefrontal cortex. Trends Neurosci. 2021;44:550–63.

56. Le Merre P, Ährlund-Richter S, Carlén M. The mouse prefrontal cortex: Unity in diversity. Neuron. 2021;109:1925–44.

57. Nelson SB, Valakh V. Excitatory/inhibitory balance and circuit homeostasis in autism spectrum disorders. Neuron. 2015;87:684–98.

58. Etherton MR, Blaiss CA, Powell CM, Südhof TC. Mouse neurexin-1alpha deletion causes correlated electrophysiological and behavioral changes consistent with cognitive impairments. Proc Natl Acad Sci USA. 2009;106:17998–8003.

59. Dong ZQ, Chen WB, Chen C, Wang HS, Cui WP, Tan ZB, et al. CUL3 deficiency causes social deficits and anxiety-like behaviors by impairing excitation-inhibition balance through the promotion of cap-dependent translation. Neuron. 2020;105:475–90.

60. Yu Y, Zhang B, Ji P, Zuo Z, Huang Y, Wang N, et al. Changes to gut amino acid transporters and microbiome associated with increased E/I ratio in Chd8+/− mouse model of ASD-like behavior. Nat Commun. 2022;13:1151.

61. Chen P, Liu Z, Zhang Q, Lin D, Song L, Liu J, et al. DSCAM deficiency leads to premature spine maturation and autism-like behaviors. J Neurosci. 2022;42:532–51.

62. Wang QW, Qin J, Chen YF, Tu Y, Xing YY, Wang Y, et al. 16p11.2 CNV gene Doc2α functions in neurodevelopment and social behaviors through interaction with secretagogin. Cell Rep. 2023;42:112691.

63. Zhang JL, Chen XL, Eaton M, Wu JX, Ma ZX, Lai SR, et al. Severe deficiency of the voltage-gated sodium channel NaV1.2 elevates neuronal excitability in adult mice. Cell Reports. 2021;36:109495.

64. John A, Ng-Cordell E, Hanna N, Brkic D, Baker K. The neurodevelopmental spectrum of synaptic vesicle cycling disorders. J Neurochem. 2021;157:208–28.

65. Yeo XY, Lim YT, Chae WR, Park C, Park H, Jung S. Alterations of presynaptic proteins in autism spectrum disorder. Front Mol Neurosci. 2022;15:1062878.

66. Yang R, Walder-Christensen KK, Kim N, Wu D, Lorenzo DN, Badea A, et al. ANK2 autism mutation targeting giant ankyrin-B promotes axon branching and ectopic connectivity. Proc Natl Acad Sci USA. 2019;116:15262–71.

67. Katrancha SM, Shaw JE, Zhao AY, Myers SA, Cocco AR, Jeng AT, et al. Trio haploinsufficiency causes neurodevelopmental disease-associated deficits. Cell Rep. 2019;26:2805. e2809

68. Tan CX, Bindu DS, Hardin EJ, Sakers K, Baumert R, Ramirez JJ, et al. δ-Catenin controls astrocyte morphogenesis via layer-specific astrocyte-neuron cadherin interactions. J Cell Biol. 2023;222:e202303138.

69. Emperador-Melero J, de Nola G, Kaeser PS. Intact synapse structure and function after combined knockout of PTPδ, PTPσ, and LAR. eLife. 2021;10:e66638.

70. Tratnjek L, Živin M, Glavan G. Synaptotagmin 7 and SYNCRIP proteins are ubiquitously expressed in the rat brain and co-localize in purkinje neurons. J Chem Neuroanat. 2017;79:12–21.

71. Yan P, Liu H, Zhou T, Sun P, Wang Y, Wang X, et al. Crosstalk of Synapsin1 palmitoylation and phosphorylation controls the dynamicity of synaptic vesicles in neurons. Cell Death Dis. 2022;13:786.

AUTHOR CONTRIBUTIONS
ZX and YJ conceived and supervised the project. YY conducted most of the experiments and analyzed the results. YL, SZ, and JS designed and performed electrophysiology experiments. YY and YL analysed the TEM results. FY is responsible for analyzing the IP-MS, Multi-SIM image, rearing test and phosphoproteomics results. YJ is responsible for analyzing the phosphoproteomics results. YX and YD contributed technical assistance for the Von-Frey behavior assays. XZ and XS contributed technical assistance for the in vivo electrophysiological recordings. XH and YW. performed the IP-MS, 6plex-TMT and phosphoproteomic assays. YY, and XZ wrote the manuscript. YL, FY, and YJ provided suggestions and revisions for the manuscript. All of the authors discussed the results and commented on the manuscript.

COMPETING INTERESTS
The authors declare no competing interests.

ETHICS APPROVAL AND CONSENT TO PARTICIPATE
The experimental procedures on mice were performed based on the protocols which were approved by the Institutional Animal Care and Use Committee at the Institute of Genetics and Developmental Biology, Chinese Academy of Sciences. The approval license number was AP2023037. No original human data was provided in this study.

ADDITIONAL INFORMATION
Supplementary information The online version contains supplementary material available at https://doi.org/10.1038/s41380-025-03370-w.

Correspondence and requests for materials should be addressed to Yisheng Jiang or Zhiheng Xu.

Reprints and permission information is available at http://www.nature.com/reprints

Publisher's note Springer Nature remains neutral with regard to jurisdictional claims in published maps and institutional affiliations.